

Luminescent Copper Halides

Near-Full-Spectrum Emission Control in Copper(I) Iodides via Inorganic Structural Engineering Within a Single-Cation Host

Yongjing Deng, Yongkang Zhu, Xiaodong Zhao, Ning Ding, Yong Yang, Mengzhu Wang, Jiangang Li, Pengfei She, Shujuan Liu, Yun Ma,* and Qiang Zhao**

Abstract: Hybrid copper(I) halides have emerged as a new class of optoelectronic materials due to their tunable structure and photophysical properties. However, systematically correlating inorganic polyhedra configurations with emission characteristics remains challenging. Herein, we address this by synthesizing a homologous series of copper(I) iodides templated solely by the $[C_{13}H_{24}N]^+$ cation. Precise control reaction conditions yielded distinct inorganic polyhedral configurations, monomeric $[CuI_3]^{2-}$ (**1**), dimeric $[Cu_2I_4]^{2-}$ (**2**), trimeric $[Cu_3I_6]^{3-}$ (**3**), and tetrameric $[Cu_4I_6]^{2-}$ (**4**). We establish a direct correlation where increasing inorganic aggregation systematically reduces the bandgap and dictates the luminescence color across a near-full visible spectrum, from blue (**1**) to cyan (**2**), red (**3**), and yellow (**4**). Detailed spectroscopic and theoretical analyses reveal the self-trapped excitons emission mechanism dependent on the Cu-I configuration, in which the closed $[Cu_4I_6]^{2-}$ configuration is more resistant to excited lattice deformation, thereby resulting in a lowest Stokes shift energy. Furthermore, stimuli-responsive sequential phase transitions between these well-defined structures were demonstrated, offering insights into their structural dynamics. This work provides critical fundamental understanding of how inorganic framework engineering within a fixed organic host precisely controls both electronic structure and excited-state relaxation pathways in hybrid copper(I) halides, paving the way for rational design of materials with tailored optical properties.

Organic-inorganic hybrid metal halides have emerged as a fascinating class of functional materials, attracting considerable attention for their diverse applications in optoelectronics, including solid-state lighting, displays, and X-ray detection.^[1-8] Among these, copper(I)-based halides stand out as particularly promising candidates due to their low toxicity, earth abundance, cost-effectiveness, and unique photoluminescence (PL) properties originating from their d^0 electronic configuration.^[9,10] A hallmark of Cu(I) halides is their remarkable structural versatility; the Cu(I) centers can coordinate with halide anions to form a wide array

of inorganic motifs, ranging from simple isolated units like $[CuX_2]^-$ rods and $[CuX_3]^{2-}$ triangles to more complex aggregates such as $[Cu_2X_4]^{2-}$ dimers, $[Cu_3X_6]^{3-}$ trimers, and $[Cu_4X_6]^{2-}$ tetrameric clusters.^[11-14] This structural diversity is intrinsically linked to their tunable PL characteristics, where emission color and mechanism often involving self-trapped excitons (STEs) are highly sensitive to the specific geometry, connectivity, and dimensionality of the inorganic copper halide framework.^[15-18]

Harnessing this inherent structure-property relationship for precise control over luminescence, particularly achieving wide-range color tunability across the visible spectrum, remains a central goal in the field. However, realizing full-color emission control, especially spanning the challenging blue-to-red region, often necessitates complex, multi-variable optimization strategies. Critically, these conventional approaches typically involve the simultaneous modification of both the organic cation (tuning its size, shape, polarity, or even electronic activity) and the inorganic anion framework (adjusting composition or connectivity).^[19-22] While effective in specific cases, this dual-component tuning complicates systematic studies and can obscure the fundamental contributions of each component. In contrast, engineering the inorganic structure systematically while utilizing a single, fixed organic cation presents a more elegant and fundamentally insightful approach.^[23-26] This strategy offers significant advantages: it simplifies material design by reducing the number of variables, and more importantly, allows for the unambiguous isolation and determination of how the inorganic architecture alone dictates the optoelectronic behavior,

[*] Y. Deng, Y. Zhu, X. Zhao, N. Ding, Y. Yang, M. Wang, J. Li, Prof. P. She, Prof. S. Liu, Prof. Y. Ma, Prof. Q. Zhao
State Key Laboratory of Flexible Electronics (LoFE) & Institute of Advanced Materials (IAM), Nanjing University of Posts & Telecommunications, Nanjing 210023, P.R. China
E-mail: pengfei.she@njupt.edu.cn
iamyma@njupt.edu.cn
iamqzhao@nuist.edu.cn

Prof. P. She, Prof. Y. Ma, Prof. Q. Zhao
College of Electronic and Optical Engineering & College of Flexible Electronics (Future Technology), Nanjing University of Posts & Telecommunications, Nanjing 210023, P.R. China

Prof. Q. Zhao
School of Electronics and Information Technology, Nanjing University of Information Science and Technology, Nanjing 210044, P.R. China

Additional supporting information can be found online in the Supporting Information section

thereby providing clearer and more direct structure-property correlations. Deciphering this intrinsic influence is crucial for rational material design. Nevertheless, achieving such precise control over the inorganic aggregation state (e.g., monomer, dimer, trimer, tetramer) using identical precursors and a fixed cation remains challenging due to the intricate nature of self-assembly processes.^[23,27–29] Establishing a homologous series of materials, differing only in the aggregation state of the inorganic unit derived from identical precursors, offers the ideal platform for systematically investigating these fundamental correlations.

To address this challenge and pursue full-color luminescence control via this targeted inorganic structural engineering strategy within a single-cation system, we report herein the rational design and synthesis of a series of heteromorphic copper iodide self-assemblies using a single, specifically chosen organic cation, $[C_{13}H_{24}N]^+$ (*N,N,N*-trimethyl-1-adamantylammonium). We selected this bulky, spherical, and polar adamantyl-based cation hypothesizing that its unique geometry could enrich the possibility and adaptability for the orientation of inorganic structural units without strongly dictating the primary luminescence pathway itself, thus allowing the influence of the inorganic structure to be clearly elucidated.^[30–32] By systematically varying solvent systems and precursor molar ratios while keeping the $[C_{13}H_{24}N]^+$ cation and Cu^+/I^- sources constant, we successfully isolated four distinct copper iodide homologs: $(C_{13}H_{24}N)_2CuI_3$ (**1**, monomer), $(C_{13}H_{24}N)_2Cu_2I_4 \cdot DMF$ (**2**, dimer), $(C_{13}H_{24}N)_3Cu_3I_6$ (**3**, trimer), and $(C_{13}H_{24}N)_2Cu_4I_6$ (**4**, tetramer). Crucially, PL measurements revealed that the luminescence behavior of these copper(I) halides is systematically related to their coordination configurations with emission wavelengths ranging from 427 to 652 nm, covering blue, cyan, yellow, and red colors. This achievement, realizing broad, near-full-spectrum emission tuning (a range of 225 nm) solely through controlled modulation of the inorganic architecture within a single-cation hybrid system, indicates the power and potential of this focused design principle. Furthermore, we discovered controllable and sequential phase transitions (**2** \leftrightarrow **3** via heat/DMF; **2** \rightarrow **4** and **3** \rightarrow **4** via MeOH) and the associated distinct, switchable emission colors (cyan \leftrightarrow red; cyan/red \rightarrow yellow). This work provides compelling evidence for the efficacy of inorganic structural engineering, enabled by rational cation selection within a single-cation framework, to achieve unprecedented control over luminescence across a major portion of the visible spectrum, advancing both fundamental understanding and potential applications.

To investigate the influence of inorganic framework aggregation on photophysical properties, a series of hybrid copper(I) iodide homologs (**1–4**) were synthesized. These compounds were derived from identical precursors, namely *N,N,N*-trimethyl-1-adamantylammonium iodide ($C_{13}H_{24}NI$) and copper(I) iodide (CuI), but were obtained under distinct reaction conditions involving variations in solvent systems and molar ratios (detailed methodologies are provided in the supporting information, Figure S1). The crystal structures of **1–4** were unequivocally determined by single-crystal X-ray diffraction (SCXRD). Compounds **1**, **2**, and **3** crystallize in monoclinic space groups, while compound **4** adopts the

cubic space group (detailed crystallographic parameters and refinement statistics are summarized in Tables S1–S12).^[33] As visualized in the packing diagrams presented in Figure 1, a common feature across all four homologs is their zero-dimensional (0D) structural characteristic at the molecular level, defined by the presence of discrete, isolated anionic copper iodide units that are not covalently linked into extended networks.^[34–36] In each case, the anionic copper iodide units are effectively spatially isolated from one another by the bulky, spherical $[C_{13}H_{24}N]^+$ organic cations. This spatial isolation ensures the optical properties are governed by the intrinsic electronic structure of each discrete anion, leading to distinct luminescence for each compound based on its specific inorganic aggregation state, Cu...Cu interactions, and electron-phonon coupling strength.

As shown in Figure 1, the inorganic component consists of discrete, isolated trigonal planar $[CuI_3]^{2-}$ monomers in **1**. The shortest intermolecular Cu...Cu distance is a considerable 8.257(2) Å, confirming there are no metal-metal interactions between adjacent inorganic anions. In **2**, two $[CuI_3]$ units undergo edge-sharing condensation to form isolated $[Cu_2I_4]^{2-}$ dimers. In **3**, three $[CuI_3]$ moieties aggregate through vertex-sharing iodine atoms, resulting in discrete $[Cu_3I_6]^{3-}$ trimers. Finally, in **4**, the inorganic framework evolves into a closed, cage-like $[Cu_4I_6]^{2-}$ tetramer. In such structure, there exist two sets of inverted Cu_4 tetrahedra, in which each Cu atom maintains a trigonal planar coordination geometry, coordinated by three I atom to form $[CuI_3]$ unit (Figure S2). These eight $[CuI_3]$ units interconnect through iodine-sharing to form $[Cu_8I_6]$ cluster. Significantly, the time-averaged superimposition of these two symmetry-related, inverted Cu_4 results in the half-weighted Cu atoms, accounting for the chemical composition of $[Cu_4I_6]^{2-}$. This systematic progression from monomer (**1**) to dimer (**2**), trimer (**3**), and tetramer (**4**) is accompanied by a dramatic variation in the intra-cluster Cu...Cu distances. While no Cu...Cu contacts exist in the monomeric **1**, the shortest Cu...Cu separations within the polynuclear clusters progressively decrease to 2.6077(10) Å in dimer **2**, 2.262(10) Å in trimer **3**, and become remarkably short at 1.974(5) Å in tetramer **4**. These distances, particularly those in **2**, **3**, and **4**, are well below the sum of van der Waals radii for copper (~2.8 Å), strongly indicating the presence and increasing strength of cuprophilic ($Cu^+ \cdots Cu^+$) interactions within these aggregated units.^[37–40] The differences in the progressive aggregation and connectivity of copper iodide anions are anticipated to significantly impact the electronic structure and excited-state dynamics.

Moreover, the phase purity of the bulk synthesized materials was rigorously verified using powder X-ray diffraction (PXRD). As depicted in Figure S3, the experimental PXRD patterns recorded for bulk samples of **1**, **2**, **3**, and **4** exhibit good agreement with the patterns simulated from their respective SCXRD-determined structures, confirming the successful and phase-pure synthesis of each targeted homolog. Lastly, X-ray photoelectron spectroscopy (XPS) was performed to determine the chemical valence states. As shown in Figures S4 and S5, the XPS peaks at 932.5 and 952.3 eV were assigned to the signal of monovalent Cu(I), indicating a negligible oxidation of Cu^+ .

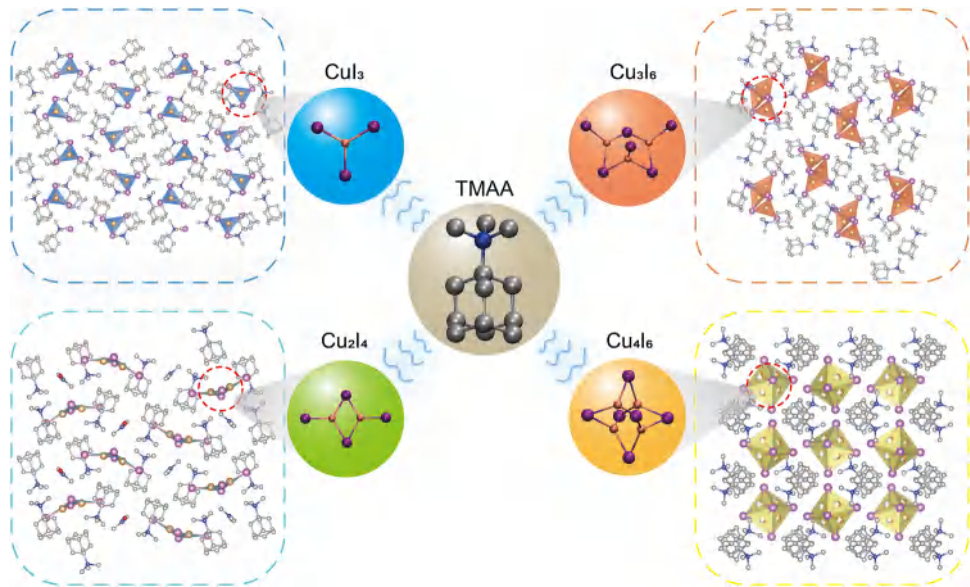


Figure 1. Schematic diagrams of crystal structures. H atoms were omitted for clarity.

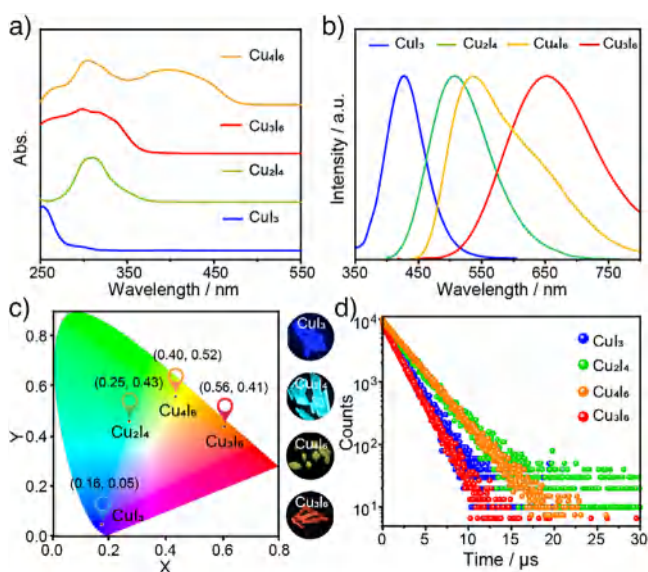


Figure 2. a) UV-vis absorption spectra, b) PL spectra, c) CIE coordinates, d) TRPL decay curve of these four compounds.

To elucidate the impact of the distinct inorganic architectures on the optical characteristics, the photophysical properties of homologs **1–4** were systematically investigated using UV-vis absorption spectroscopy, steady-state PL, and photoluminescence excitation (PLE) measurements at room temperature. The UV-vis absorption spectra (Figure 2a) reveal that compounds **1**, **2**, and **3**, containing monomeric, dimeric, and trimeric copper iodide units, respectively, exhibit minimal absorption in the visible region, consistent with their colorless appearance. In contrast, compound **4**, featuring the tetrameric $[Cu_4I_6]^{2-}$ cluster, displays a significantly extended absorption edge reaching into the visible spectrum. This trend is quantified by their corresponding optical bandgaps (E_g)

(Figure S6), which progressively decrease with increasing inorganic unit aggregation: E_g values were determined to be 4.23 eV for **1**, 3.71 eV for **2**, 3.49 eV for **3**, and markedly lower at 2.68 eV for **4**. This systematic redshift of the absorption edge correlates directly with the increasing degree of inorganic framework condensation and the associated shortening of intra-cluster Cu···Cu distances (as discussed in the structural analysis), suggesting enhanced electronic coupling and delocalization within the larger polynuclear units.^[28,29,41,42] Under UV excitation, the four homologs exhibit strikingly different emission colors, vividly demonstrating the profound influence of the inorganic structure. Steady-state PL and PLE spectra are presented in Figures 2b and S7. Monomer **1** displays a pronounced blue emission centered at 427 nm, with a full width at half-maximum (FWHM) of 72 nm. Dimer **2** shows a cyan emission peaking at 505 nm and features a broader FWHM of 111 nm. The emission of trimer **3** is further red-shifted, presenting a low-energy red emission centered at 652 nm and characterized by an increased FWHM of 169 nm. Notably, tetramer **4** deviates from a simple monotonic redshift trend relative to its aggregation size, displaying a broad, Gaussian asymmetric yellow emission peaking at 536 nm. This remarkable spectral progression from blue (427 nm) to cyan (505 nm), red (652 nm), and yellow (536 nm) indicates the successful tuning of luminescence across a wide visible range ($\Delta\lambda \approx 225$ nm) primarily driven by the engineered aggregation state of the copper iodide framework. The corresponding Commission Internationale de l'Eclairage (CIE) chromaticity coordinates visually represent this color evolution: (0.16, 0.05) for **1**, (0.25, 0.43) for **2**, (0.56, 0.41) for **3**, and (0.40, 0.52) for **4** (Figure 2c). Furthermore, these materials exhibit notable luminescence efficiencies at room temperature. The photoluminescence quantum yields (PLQY) were determined to be 50.3% for **1**, 98.3% for **2**, 31.6% for **3**, and 85.6% for **4** (Figure S8).

To gain deeper insights into the excited-state dynamics and elucidate the origins of the distinct emissions observed in homologs **1–4**, time-resolved photoluminescence (TRPL) decay measurements and temperature-dependent PL spectroscopy were conducted. TRPL decay curves were monitored at the respective maximum emission wavelengths at room temperature (Figure 2d). For the blue-emitting monomer **1**, cyan-emitting dimer **2**, red-emitting trimer **3**, and yellow-emitting tetramer **4**, the PL decay follows a mono-exponential function, yielding lifetimes (τ) of 1.75, 1.97, 1.68, and 2.63 μ s, respectively. The microsecond-scale lifetimes, in conjunction with the broad FWHM and large Stokes shift conform to the characteristics of STEs emission.^[15,43] Further confirmation of the emission origin was sought by examining excitation-wavelength-dependent PL spectra. As shown in Figure S9, the emission spectral profiles for each individual compound remain largely unchanged upon varying the excitation wavelength. This observation strongly suggests that the broadband emission in each case originates from the relaxation of the same lowest excited state (or a set of closely coupled states) generated after excitation, regardless of the initial excitation energy.^[20,21,44]

The influence of temperature on the PL properties provides critical information about electron-phonon coupling and excited-state relaxation pathways (Figure S10). For monomer **1** and dimer **2**, cooling from 300 to 80 K results in a gradual increase in PL intensity and a slight narrowing of the emission band, without the appearance of new peaks. This behavior is typical of thermally activated non-radiative decay suppression and is consistent with emission originating from a single primary radiative pathway (STE state).^[26] The observed decrease in intensity and broadening of FWHM upon heating from 80 K confirms the significant role of electron-phonon coupling.^[45,46] Trimer **3** displays more complex behavior. As temperature decreases from 300 K to approximately 220 K, the red emission intensity increases similarly to **1** and **2**. However, upon further cooling below 220 K, the spectra exhibit a marked alteration, showing a new near-infrared emission peak centered at 745 nm. This luminescence evolution stems from the temperature-induced structural phase transition, which is confirmed by the corresponding single crystal structure at 150 K (Tables S13–S15, Figure S11). Tetramer **4** shows a continuous increase in emission intensity upon cooling from 300 to 80 K, consistent with the suppression of non-radiative pathways. Notably, the Gaussian asymmetric emission clearly splits into dual emission peaks at low temperatures, centered at approximately 536 and 649 nm. The lifetimes for both peaks recorded at 80 K are highly comparable and both undergo a mono-exponential decay kinetics, while longer overall lifetimes compared to 300 K due to reduced non-radiative recombination (Figure S12). These results suggest that the double emission phenomenon may originate from the relaxation processes of discrete excited states.^[28]

To correlate the observed photophysical behavior with electronic structures, density functional theory (DFT) calculations were performed. Projected density of states (PDOS) analyses reveals similarities and differences (Figure 3a–d). For all homologs, the valence band maximum (VBM) is primarily

composed of hybridized Cu-*d* and I-*p* orbitals. However, the composition of the conduction band minimum (CBM) varies significantly with the inorganic structure. In monomer **1**, the CBM involves contributions from both Cu-*s* states and orbitals associated with the $[\text{C}_{13}\text{H}_{24}\text{N}]^+$ organic cation. In contrast, the CBM for dimer **2** and trimer **3** are predominantly localized on the inorganic Cu-I clusters, mainly involving Cu-*s* and I-*p* orbitals, while the CBM for tetramer **4** are dominated by Cu-*p* and I-*p* orbitals. This imply that the Cu...Cu interaction intensifies with the increase of inorganic aggregation, which is consistent with the shortened Cu...Cu distance and might account for the reduced bandgap.^[37,47] Moreover, the partial charge density distribution show that electrons and holes are localized on the inorganic Cu-I clusters for all homologs, which matches well with the STEs emission mechanisms (Figures S13–S16).^[21] In 0D hybrid metal halides, anionic inorganic polyhedrons are isolated and spatially surrounded by organic cations. Under photoexcitation, the photogenerated excitons are subsequently trapped by this soft lattice to form STEs, accompanying with transient elastic lattice deformations and some energy loss. Thus, the radiative recombination of STEs result in broadband emission with large Stokes shifts.^[15,43,48]

To reveal the distinct luminescent behaviors dependent on the Cu-I configurations, the configurational coordinate diagrams of these four homologs were calculated to illustrate the formation of STEs. The emission energy was calculated as

$$E_{PL} = E_g - E_b - E_{st} - E_d$$

where E_b is the exciton binding energy, E_{st} is the self-trapping energy, and E_d is the lattice-deformation energy.^[49,50] As shown in Figure 3e,f and Table S16, the trends of the Stokes shift energy and emission energy are basically consistent with the experimental values. As the inorganic framework evolved from the isolated $[\text{CuI}_3]^{2-}$ monomer in **1** to the $[\text{Cu}_2\text{I}_4]^{2-}$ dimer in **2**, and the $[\text{Cu}_3\text{I}_6]^{3-}$ trimer in **3**, the Stokes shift energy gradually increases and the emission energy decreases accordingly, which might be attributed to the enhanced Cu...Cu interaction. Notable, tetramer **4** instead possess the smallest Stokes shift energy despite the shortest Cu...Cu distance. This might be due to the fact that the closed configuration is more resistant to the excited-state lattice deformation, which can be demonstrated by the lowest coordinate difference ΔQ (the lattice changes between the ground- and excited-state equilibrium position).^[22]

Beyond their distinct static photophysical properties, these copper iodide homologs exhibit fascinating stimuli-responsive behavior, enabling sequential and controllable phase transitions between different members of the series, accompanied by dramatic luminescence color switching (Figure 4a). Specifically, upon heating at 100 °C, the cyan-emitting compound **2** gradually transforms into a red-emitting species, the emission profile of which matches that of compound **3** (Figure 4b). The PXRD pattern of the heated sample matches the simulated pattern of compound **3**, revealing the thermally induced phase transition from **2** to **3** (Figure 4c). The thermogravimetric analysis (TGA) results indicate this transition involves the release of DMF molecules from the crystal lattice

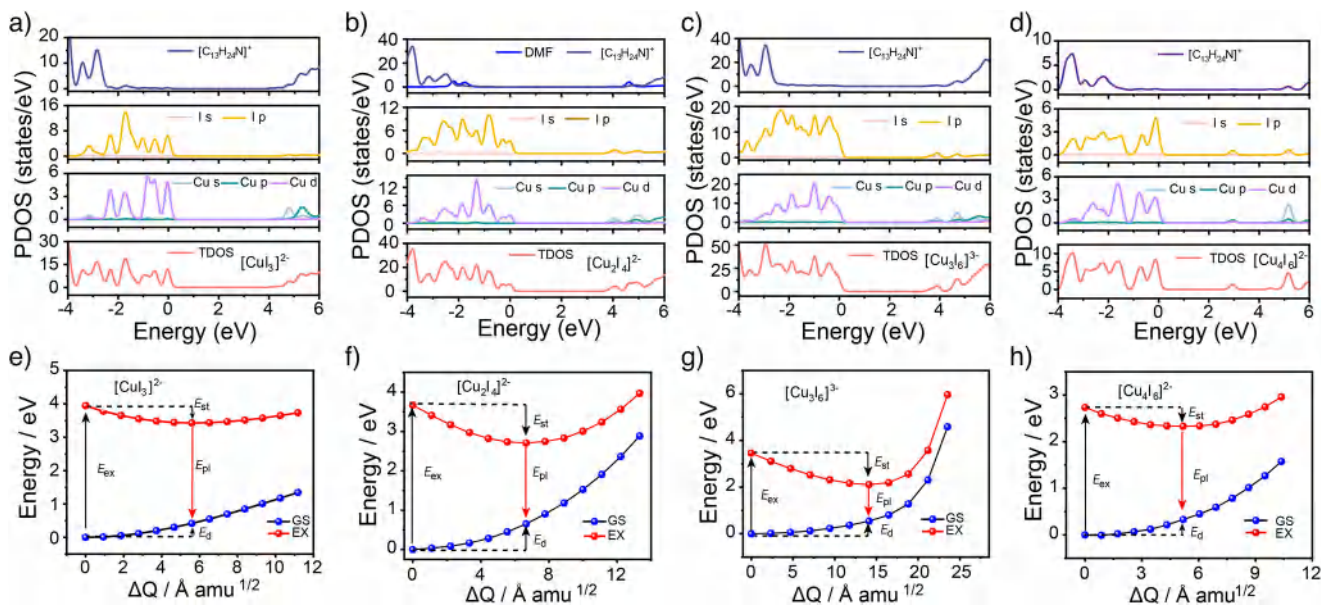


Figure 3. a-d) Projected density of states (PDOS) of compound 1–4. e–h) Configuration coordinate diagram for the STEs formation of compound 1–4.

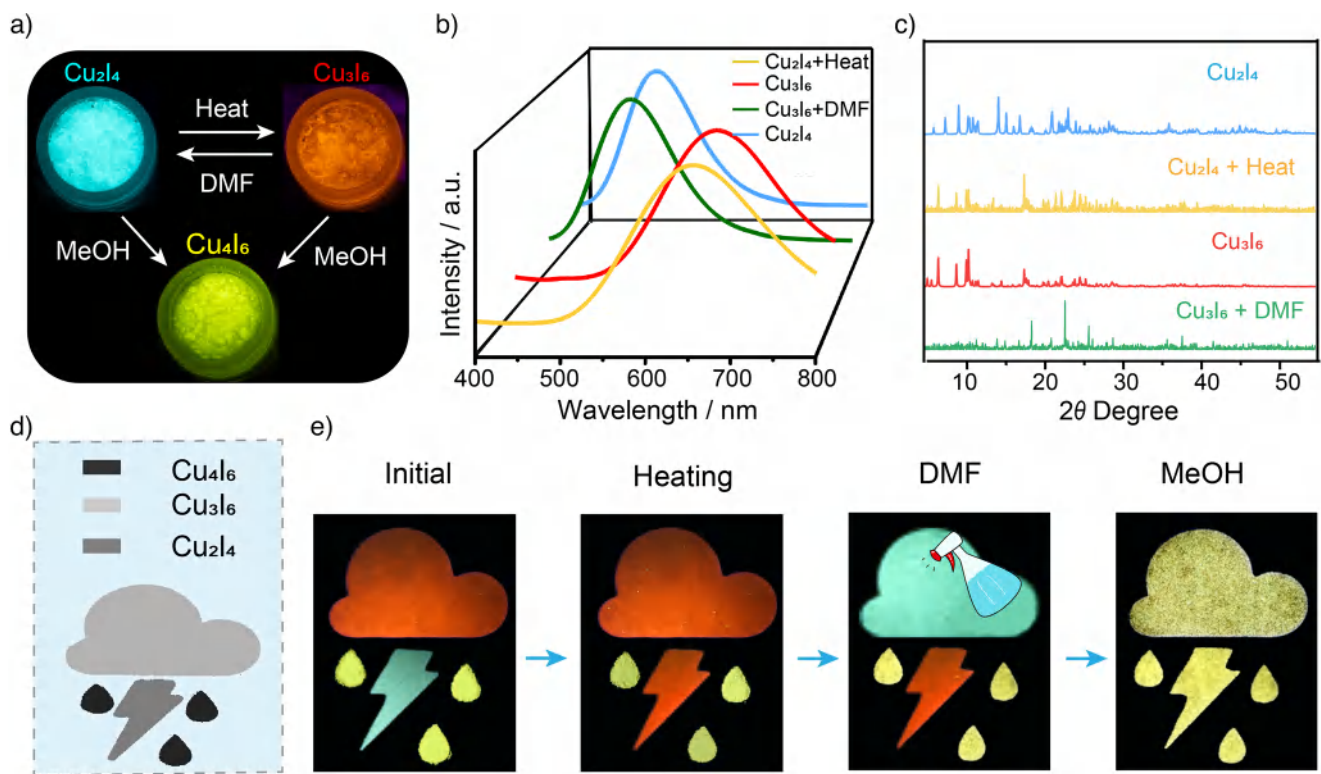
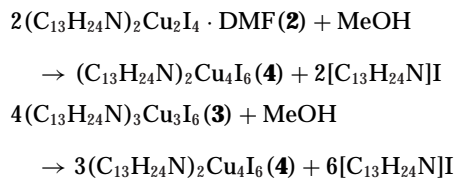


Figure 4. a) Images, b) the corresponding PL spectra, and c) XRD pattern for the sequential phase transitions process, d) anti-counterfeiting demo: Photo images of security patterns under 365 nm ultraviolet light.

(Figure S17). Intriguingly, when exposed to DMF, the red-emitting compound **3** undergoes gradual transformation into the cyan-emitting species, that is, compound **2**, as unequivocally confirmed by corresponding PL emission spectra and PXRD. Furthermore, solvent treatment with methanol can induce transitions towards the most aggregated tetramer

phase. When either the cyan-emitting dimer **2** or the red-emitting trimer **3** is exposed to methanol, both gradually transform into a yellow-emitting species (Figure S18a). In situ PXRD analysis were performed to reveal these processes, identifying the yellow-emitting product as a mixture of phases $(C_{13}H_{24}N)_2Cu_4I_6$ and $[C_{13}H_{24}N]I$ (Figure S18b). The

observed phase transitions arise from the ion pair dissociation promoted by methanol (polar protic solvent). Given the ionic lattice characteristics of hybrid copper(I) halides, once exposed to methanol, the organic cations are preferentially dissociated due to the high solubility. Correspondingly, the phase transition from $[\text{Cu}_2\text{I}_4]^{2-}$ or $[\text{Cu}_3\text{I}_6]^{3-}$ to $[\text{Cu}_4\text{I}_6]^{2-}$ will occur to maintain charge neutrality. These solvent-induced transformations can be represented by the following chemical equations:



These controllable, sequential phase transitions ($\mathbf{2} \leftrightarrow \mathbf{3}$ via heat/DMF; $\mathbf{2} \rightarrow \mathbf{4}$ and $\mathbf{3} \rightarrow \mathbf{4}$ via MeOH) and the associated distinct, switchable emission colors (cyan \leftrightarrow red; cyan/red \rightarrow yellow) stimulate a proof-of-concept demonstration for advanced security applications. To demonstrate this, a multi-level anti-counterfeiting demonstration was designed (Figure 4d). Phosphor powders of **2** (cyan), **3** (red), and **4** (yellow) were patterned into distinct shapes (lightning, cloud, and raindrop, respectively) within a mold. Initially, under 365 nm UV excitation, the patterns display their intrinsic cyan, red, and yellow colors. Upon applying a uniform heating treatment to the entire demo, only the “lightning” pattern (**2**) changes color, transforming to red (**3**), while the others remain unchanged. This provides a first level of authentication. Subsequently, selectively applying DMF solvent to the “cloud” pattern (**3**) causes it to transform into cyan emission (**2**), adding another security layer. Finally, treating the entire pattern with methanol results in all components exhibiting yellow emission, as both **2** and **3** convert to **4**. Throughout this dynamic process, the “raindrop” (**4**) acts as a stable reference, while the “lightning” and “cloud” patterns exhibit tunable, multi-color responses depending on the sequence of thermal and solvent stimuli. This allows for encoding complex information through the specific color states induced by different treatments.

In conclusion, this work successfully addressed the challenge of achieving broad emission tunability in hybrid copper(I) halides via systematic inorganic framework engineering within a single-cation host system. We successfully synthesized a homologous series of 0D hybrid copper(I) iodides templated by $[\text{C}_{13}\text{H}_{24}\text{N}]^+$, featuring distinct inorganic anions from monomeric $[\text{CuI}_3]^{2-}$ to tetrameric $[\text{Cu}_4\text{I}_6]^{2-}$. A clear structure-property relationship was established, increasing inorganic aggregation systematically redshifts absorption edges and enables remarkable luminescence tuning across the visible spectrum, from blue to cyan, red, and yellow. Spectroscopic and theoretical studies revealed the fascinating STEs mechanism dependent on the Cu-I coordination configuration. Furthermore, controllable, sequential phase transitions between homologs were demonstrated, triggered by thermal and solvent stimuli. These transitions induce

dynamic, switchable luminescence colors, successfully applied in a multi-level anti-counterfeiting demonstration.

Acknowledgements

This work was supported by the National Natural Science Foundation of China (62322508, 62288102 and 62075101), Funded by Basic Research Program of Jiangsu (BK20243057), the Postdoctoral Fellowship Program of CPSF (GZC20240744), Jiangsu Funding Program for Excellent Postdoctoral Talent (2024ZB133 and 2024ZB087), China Postdoctoral Science Foundation (2024M751502 and 2024M761489).

Conflict of Interests

The authors declare no conflict of interest.

Data Availability Statement

The data that support the findings of this study are available in the Supporting Information of this article.

Keywords: Anti-counterfeiting • Configurations • Metal halide • Self-trapped excitons • Sequential phase transition

-
- [1] L. Mao, J. Chen, P. Vishnoi, A. K. Cheetham, *Acc. Mater. Res.* **2022**, *3*, 439–448.
 - [2] L. Yuan, Q. Xue, F. Wang, N. Li, G. I. N. Waterhouse, C. J. Brabec, F. Gao, K. Yan, *Chem. Rev.* **2025**, *125*, 5057–5162.
 - [3] Y. Deng, X. Liang, F. Li, M. Wang, Z. Zhou, J. Zhao, F. Wang, S. Liu, Q. Zhao, *Laser Photonics Rev.* **2023**, *17*, 2300043.
 - [4] B. Zhou, F. Fang, Z. Liu, H. Zhong, K. Zhou, H. Hu, J. Min, F. Zheng, S. Fang, J. Nie, J. Huang, L. Li, H. Li, Y. Wan, Y. Shi, *J. Am. Chem. Soc.* **2024**, *146*, 15198–15208.
 - [5] X. He, Y. Deng, D. Ouyang, N. Zhang, J. Wang, A. A. Murthy, I. Spanopoulos, S. M. Islam, Q. Tu, G. Xing, Y. Li, V. P. Dravid, T. Zhai, *Chem. Rev.* **2023**, *123*, 1207–1261.
 - [6] P. Tao, S. Liu, W. Y. Wong, *Adv. Opt. Mater.* **2020**, *8*, 2000985.
 - [7] R. Xing, Z. Li, W. Zhao, D. Wang, R. Xie, Y. Chen, L. Wu, X. Fang, *Adv. Mater.* **2024**, *36*, 2310248.
 - [8] Z. Zhao, Z. Hu, M. Deng, E. Hong, P. Wang, Z. Li, X. Fang, *Adv. Mater.* **2025**, *37*, 2416033.
 - [9] J. Wen, K. Rong, L. Jiang, C. Wen, B. Wu, B. Sa, Y. Qiu, R. Ahuja, *Nano Energy* **2024**, *128*, 109802.
 - [10] Z. Ma, X. Ji, S. Lin, X. Chen, D. Wu, X. Li, Y. Zhang, C. Shan, Z. Shi, X. Fang, *Adv. Mater.* **2023**, *35*, 2300731.
 - [11] D. Huang, C. Cao, H. Cheng, D. Wang, W. Yang, R. Xie, *Mater. Today Chem.* **2024**, *37*, 102010.
 - [12] R. An, Q. Wang, Y. Liang, P. Du, P. Lei, H. Sun, X. Wang, J. Feng, S. Song, H. Zhang, *Angew. Chem. Int. Ed.* **2025**, *64*, e202413991.
 - [13] L. Lian, T. Zhang, H. Ding, P. Zhang, X. Zhang, Y. Zhao, J. Gao, D. Zhang, Y. Zhao, J. Zhang, *ACS Mater. Lett.* **2022**, *4*, 1446–1452.
 - [14] Z. Liu, Z. Liu, L. Xie, N. Lv, H. Yang, H. Pi, X. Li, S. Li, Z. Lin, B. Chen, *Adv. Opt. Mater.* **2025**, *13*, 2402304.
 - [15] D. A. Popov, B. Saparov, *J. Mater. Chem. C* **2025**, *13*, 521–560.

- [16] Y. Li, Z. Zhou, F. K. Sheong, Z. Xing, R. Lortz, K. S. Wong, H. H. Y. Sung, I. D. Williams, J. E. Halpert, *ACS Energy Lett.* **2021**, *6*, 4383–4389.
- [17] X. Liu, Y. Li, T. Liang, W. Liu, J. Fan, *J. Phys. Chem. Lett.* **2022**, *13*, 1373–1381.
- [18] Z. Zang, X. Yang, X. Yang, Z. Liu, Q. Qian, S. M. H. Qaid, A. S. Aldwayyan, B. Wang, S. Zhao, *Adv. Opt. Mater.* **2025**, *13*, 2403177.
- [19] D. Banerjee, B. Saparov, *Chem. Mater.* **2023**, *35*, 3364–3385.
- [20] T. Xu, Y. Li, M. Nikl, R. Kucerkova, Z. Zhou, J. Chen, Y. Sun, G. Niu, J. Tang, Q. Wang, G. Ren, Y. Wu, *ACS Appl. Mater. Interfaces* **2022**, *14*, 14157–14164.
- [21] D. A. Popy, Y. Singh, Y. Tratsiak, A. M. Cardoza, J. M. Lane, L. Stand, M. Zhuravleva, N. Rai, B. Saparov, *Aggregate* **2024**, *5*, e602.
- [22] L. Xiong, H. Jiang, *J. Phys. Chem. C* **2025**, *129*, 2036–2043.
- [23] J. Lai, C. Li, Z. Wang, L. Guo, Y. Wang, K. An, S. Cao, D. Wu, Z. Liu, Z. Hu, Y. Leng, J. Du, P. He, X. Tang, *Chem. Eng. J.* **2024**, *494*, 153077.
- [24] J. Wu, Q. Huang, Y. Fu, L. Qi, L. Chen, S. Yan, W. Liu, S. Guo, *Angew. Chem. Int. Ed.* **2025**, *64*, e202506748.
- [25] S. Chen, J. Gao, J. Chang, Y. Li, C. Huangfu, H. Meng, Y. Wang, G. Xia, L. Feng, *ACS Appl. Mater. Interfaces* **2019**, *11*, 17513–17520.
- [26] D. Li, J. Wu, X. Wang, X. Zhang, C. Yue, X. Lei, *Chem. Mater.* **2023**, *35*, 6598–6611.
- [27] X. Liu, B. Li, J. Jin, L. Yang, Z. Xia, Y. Xu, *Chem. Commun.* **2024**, *60*, 9034–9037.
- [28] S. Cao, J. Lai, Y. Wang, K. An, T. Jiang, M. Wu, P. Feng, P. He, X. Tang, *Laser Photonics Rev.* **2024**, *18*, 2400799.
- [29] J. Wu, J. Qi, Y. Guo, S. Yan, W. Liu, S. Guo, *Inorg. Chem. Front.* **2023**, *11*, 156–163.
- [30] J. Zhou, S. Jin, C. Chai, M. Hao, X. Zhong, T. Ying, J. Guo, X. Chen, *Innovation* **2022**, *3*, 100204.
- [31] Z. Wang, D. Xie, F. Zhang, J. Yu, X. Chen, C. P. Wong, *Sci. Adv.* **2020**, *6*, eabc2181.
- [32] T. Shao, R. Ren, P. Huang, H. Ni, C. Su, D. Fu, Y. Xie, H. Lu, *Dalton Trans.* **2022**, *51*, 2005–2011.
- [33] Deposition Numbers 2466546 (for (C13H24N)2CuI3), 2466548 (for (C13H24N)2Cu2I4•DMF), 2466547 (for (C13H24N)3Cu3I6), 2466549 (for (C13H24N)2Cu4I6), and 2466341 (for (C13H24N)3Cu3I6-150 K) contains the supplementary crystallographic data for this paper. These data are provided free of charge by the joint Cambridge Crystallographic Data Centre and Fachinformationszentrum Karlsruhe Access Structures service.
- [34] C. Zhou, H. Lin, Q. He, L. Xu, M. Worku, M. Chaaban, S. Lee, X. Shi, M.-H. Du, B. Ma, *Mater. Sci. Eng. R-Rep.* **2019**, *137*, 38–65.
- [35] M. Li, Z. Xia, *Chem. Soc. Rev.* **2021**, *50*, 2626–2662.
- [36] K. Zhu, O. Reid, S. Rangan, L. Wang, J. Li, K. A. J. Durai, K. Zhou, N. Javed, L. Kasaei, C. Yang, M. Li, Y. Sun, K. Tan, M. Cotlet, Y. Liu, L. C. Feldman, D. M. O'Carroll, K. Zhu, J. Li, *Nature* **2025**, *643*, 1246.
- [37] S. Wang, Z. Yang, X. Sun, M. Wu, K. Sheng, L. Zhang, B. Yang, K. Wang, Y. Sui, B. Zou, *Angew. Chem. Int. Ed.* **2025**, *64*, e202414810.
- [38] S. Maderlehner, M. J. Leitl, H. Yersin, A. Pfitzner, *Dalton Trans.* **2015**, *44*, 19305–19313.
- [39] J. Chatterjee, A. Chatterjee, R. Tanwar, P. Panwarria, S. Saikia, M. D. Ambhore, P. Mandal, P. Hazra, *J. Phys. Chem. Lett.* **2024**, *15*, 6069–6080.
- [40] Q. Hu, C. Zhang, X. Wu, G. Liang, L. Wang, X. Niu, Z. Wang, W. Si, Y. Han, R. Huang, J. Xiao, D. Sun, *Angew. Chem. Int. Ed.* **2023**, *62*, e202217784.
- [41] Q. Li, B. Xu, Z. Quan, *Acc. Chem. Res.* **2023**, *56*, 3282–3291.
- [42] C. Sun, Z. Deng, Z. Li, Z. Chen, X. Zhang, J. Chen, H. Lu, P. Canepa, R. Chen, L. Mao, *Angew. Chem. Int. Ed.* **2023**, *62*, e202216720.
- [43] J. Yao, H. Liu, Z. Chen, B. Ma, L. Xu, *Angew. Chem. Int. Ed.* **2025**, *64*, e202423185.
- [44] L. Lian, P. Zhang, J. Gao, D. Zhang, J. Zhang, *Chem. Mater.* **2023**, *35*, 9339–9345.
- [45] D. Li, Q. Tan, M. Ren, W. Wang, B. Zhang, G. Niu, Z. Gong, X. Lei, *Sci. China Mater.* **2023**, *66*, 4764–4772.
- [46] Y. Zhu, X. Liang, X. Zhao, H. Cui, A. Yu, K. Y. Zhang, S. Liu, F. Wang, Q. Zhao, *Laser Photonics Rev.* **2025**, *19*, 2401802.
- [47] H. Lim, M. T. Brueggemeyer, W. J. Transue, K. K. Meier, S. M. Jones, T. Kroll, D. Sokaras, B. Kelemen, B. Hedman, K. O. Hodgson, E. I. Solomon, *J. Am. Chem. Soc.* **2023**, *145*, 16015–16025.
- [48] L. Zhou, J. F. Liao, D. B. Kuang, *Adv. Opt. Mater.* **2021**, *9*, 2100544.
- [49] C. Wei, S. Dong, Z. Xu, M. Li, T. Zhang, Z. Xu, S. Lan, S. Wang, L. Mao, *Angew. Chem. Int. Ed.* **2024**, *63*, e202412253.
- [50] J. Luo, X. Wang, S. Li, J. Liu, Y. Guo, G. Niu, L. Yao, Y. Fu, L. Gao, Q. Dong, C. Zhao, M. Leng, F. Ma, W. Liang, L. Wang, S. Jin, J. Han, L. Zhang, J. Etheridge, J. Wang, Y. Yan, E. H. Sargent, J. Tang, *Nature* **2018**, *563*, 541–545.

Manuscript received: July 02, 2025

Revised manuscript received: August 08, 2025

Accepted manuscript online: August 17, 2025

Version of record online: ■ ■ ■